ELSEVIER

Check for updates

Reaching near-theoretical strength by achieving quasi-homogenous surface dislocation nucleation in MgO particles

Sijing Chen [1,#], Fei Liu [2,#], Boyu Liu [2,*], Xiao Chen [3], Xiaoxing Ke [4], Manchen Zhang [4], Xiaochang Tang [5], Pengfei Guan [6], Ze Zhang [1], Zhiwei Shan [2], Qian Yu [1,*]

[1] Department of Materials Science & Engineering, Center of Electron Microscopy and State Key Laboratory of Silicon Materials, Zhejiang University, Hangzhou 310027, China
[2] Center for Advancing Materials Performance from the Nanoscale (CAMP-Nano) and Hysitron Applied Research Center in China (HARCC), State Key Laboratory for Mechanical Behavior of Materials, Xi'an Jiaotong University, Xi'an 710049, China
[3] Beijing Key Laboratory of Green Chemical Reaction Engineering and Technology, Department of Chemical Engineering, Tsinghua University, Beijing 100084, China
[4] Beijing Key Laboratory of Microstructure and Properties of Solids, Faculty of Materials and Manufacturing, Beijing University of Technology, Beijing 100124, China
[5] Institute of Physics, Chinese Academy of Sciences, Beijing 100190, China
[6] Beijing Computational Science Research Center, Beijing 100193, China

The structural stability of the ceramic nanoparticle (NP) is essential for its versatile applications in broad fields. Due to inevitable imperfections on the surfaces, the NP usually yields at a stress that is far below its theoretical strength. Here we propose an effective way to approach the theoretical strength of the NPs by simply homogenizing the primary imperfections. Electron beam irradiation is utilized to modify the original uneven surface and achieve surface nano-crystallization in MgO NPs, which leads to more homogeneous stress distribution intrinsically as proved by numerical simulations. As a result, quasi-homogeneous surface nucleation of dislocations occurs and raises the compressive strength to be three times higher than the as-received particles with the original surface. The near-theoretical strength gained here indicates that the imperfection in materials can be homogenized to optimize the properties to approach that of perfect crystals.

Keywords: Nanomaterial; Mechanical property; In-situ TEM; Surface treatment; Dislocation nucleation

Introduction

With the fast development of nanotechnology and growing precision in industry production, ceramic NPs with large specific surface areas have gained increasing attention in broad fields including medicine, physics, optics, and electronics [1,2]. The successful applications in these fields raise the need for a deep understanding of the basics of their structural stability under any applied external forces, which is usually highly relevant to the shape, size, and surface conditions of individual particles [3–6], the mechanical properties of ceramic NPs have been the subject of extensive studies over the past decades.

Unlike bulk materials, wherein pre-existing dislocations are inevitable during the synthesis process, nanomaterials usually have much fewer or even zero defects due to extremely small volumes and near-equilibrium crystal growth. Therefore, dislocation nucleation plays a vital role in the deformation of nanomaterials [7]. Understanding the dislocation nucleation mechanism is the key to controlling the mechanical properties of defect-free specimens. Dislocation nucleation largely depends on the surface conditions. For instance, molecular dynamics (MD) simulations

* Corresponding authors.
E-mail addresses: Liu, B. (boyuliu@xjtu.edu.cn), Yu, Q. (yu_qian@zju.edu.cn).
# These authors contributed equally.

1369-7021/© 2022 Elsevier Ltd. All rights reserved. https://doi.org/10.1016/j.mattod.2022.04.007

show that surface roughness can lead to different deformation mechanisms, in which the atomic steps on the surface will generate stress gradients and act as preferable nucleation sites for defects, resulting in scattered flow stresses [8], while the variation of nucleation stress can be quite large if the surface undulation is not uniform. However, it has been challenging to quantitatively study surface dislocation nucleation in pristine crystals. Most of the studies concerning dislocation nucleation are based on calculation and atomistic simulations but lack experimental information and proof [9–14]. How to experimentally tune the surface condition to optimize the mechanical properties and structural stability of ceramic NPs through the modulation of such surface nucleation-controlled plasticity remains interesting and to be explored.

Here, MgO is chosen as the studying subject. The dislocation nucleation-controlled mechanical behaviors of MgO NPs and their influence by surface treatment through electron beam (E-beam) was investigated by using transmission electron microscope (TEM) characterizations, high-angle annular dark-field scanning transmission electron microscopy (HAADF-STEM), three-dimensional (3D) electron tomography and in-situ compression tests inside TEM. It is discovered that the original MgO NP has uneven surface that causes stress concentration, heterogeneous dislocation nucleation under loading and therefore failure of MgO NP at a strength that is far below the theoretical strength [15]. After surface treatment by electron irradiation, dense nanostructures uniformly form on the surface. The surface treatment homogenizes the original imperfections on the surface, which not only prevent stress localization, but also promote multiple surface dislocation nucleation. As a result, the modified MgO NPs reach a strength that is nearly three times that of the original ones. The finite element method is also utilized to simulate the stress state of MgO nanoparticles with different surface conditions. It indicates that samples with closely distributed smaller bumps display more homogeneous stress distribution compared to samples with sparsely distributed large bumps, which is consistent with the experimental results.

Results

All the MgO NPs are prepared by burning the pure Mg strip in the air and collecting the smoke. It is a method known to produce cubic shape NPs. The MgO NP was first characterized by TEM, EDS mapping, and 3D electron tomography. As displayed in the bright-field TEM image in Fig. 1a, the MgO NPs are cubic with sharp edges and corners. The diameter of the MgO NPs ranges from tens to hundreds of nanometers, providing different sizes of samples for the in-situ compression tests. The fast Fourier transform (FFT) pattern and high-resolution TEM (HRTEM) images in Fig. 1b show the FCC crystal structure of the MgO NPs. It can be seen that the NP is terminated by their {100} crystal planes. The cubic shape and the terminating planes are consistent with previous calculations and simulations that both verify the high thermodynamic stability of MgO NPs of cubic shape with {100} terminations [16,17]. Since the {100} crystal planes of MgO are neutral planes composed of magnesium ions and oxygen ions in a ratio of 1:1 and have no polarity, most MgO NPs take the neutral plane {100} as the final surface. Further, no contrast of defects such as dislocations, twinning, or grain boundaries can be seen in the TEM images, even when the zone axis is tilted. Therefore, similar samples used for the following in-situ compression tests are considered to be initially dislocation-free. The chemical components of the NPs are confirmed by the EDS mapping in Fig. 1c, which shows that the elements in the MgO NPs are uniformly distributed, with no significant contaminations and no obvious chemical segregation.

Since TEM images are only two-dimensional projections of the real shape, which cannot fully describe the surface morphology, 3D electron tomography was used to reconstruct the surface morphology of the NPs in 3D. The reconstructed 3D tomogram in Fig. 1d gives more comprehensive 3D morphologic information on the MgO NP. The results indicate that the NPs are cubic-shaped, which is consistent with previous TEM characterization. However, the surface was found to be rather rough with surface undulations. In practical applications, these raised areas on the surface may cause stress concentration when being loaded.

As the MgO NP can be easily modified by electron irradiation, the E-beam is utilized to improve the surface structure and tune the surface roughness of MgO. The time-sequence HRTEM images in Fig. 2a and b illustrate the surface nanocrystallization process of MgO NPs under electron irradiation from different perspectives. It is discovered that, under the E-beam (voltage 200 keV, dose rate 4620 e/Å^{2}s), homogeneously distributed nanoscale brick-like nanostructures with {100} facets formed on the surface of the NP. Fig. 2b shows the formation of these nanostructures from a different view. The surface atoms shrink inward layer by layer, forming high-density, uniformly distributed cubic nanostructures on the surface gradually, which unifies the originally raised areas. These nanostructures are dominated by {100} non-polar crystal planes. {111} planes can also be occasionally observed during the electron irradiation process, but they will eventually evolve to {100} planes as they are polar planes for MgO which have high energy [16]. It was also found that the originally raised areas are preferentially subducted under electron irradiation, which promotes the homogenization of the surface, as shown in Fig. S1.

Radiolysis damage and displacement damage are two main irradiation damage mechanisms. The former results from the decay of electronic excitations during the irradiation and the latter involves the elastic collision of incident particles and target atoms. It is believed that displacement damage is the main irradiation damage mechanism for MgO [18]. Previous calculations show that the energy required to displace the Mg and O atoms in the interior of MgO crystals is three times higher than the displacement energy for the atoms (ions) or molecules at defect sites on the MgO surfaces under 200 keV [19]. Here in the experiment, it is found that the electron irradiation dose used in the experiment can modify the surface of MgO particles without changing their internal crystal structure. The entire crystal structure of the MgO NPs maintained under electron irradiation.

However, it is worth noting that the degree to which MgO NPs are affected by electron radiation is different. The impact of electron irradiation on the surface of the MgO NP was found to be sample size-related. As indicated by the left HRTEM images in Fig. 2c, NPs larger than 100 nm were barely influenced under

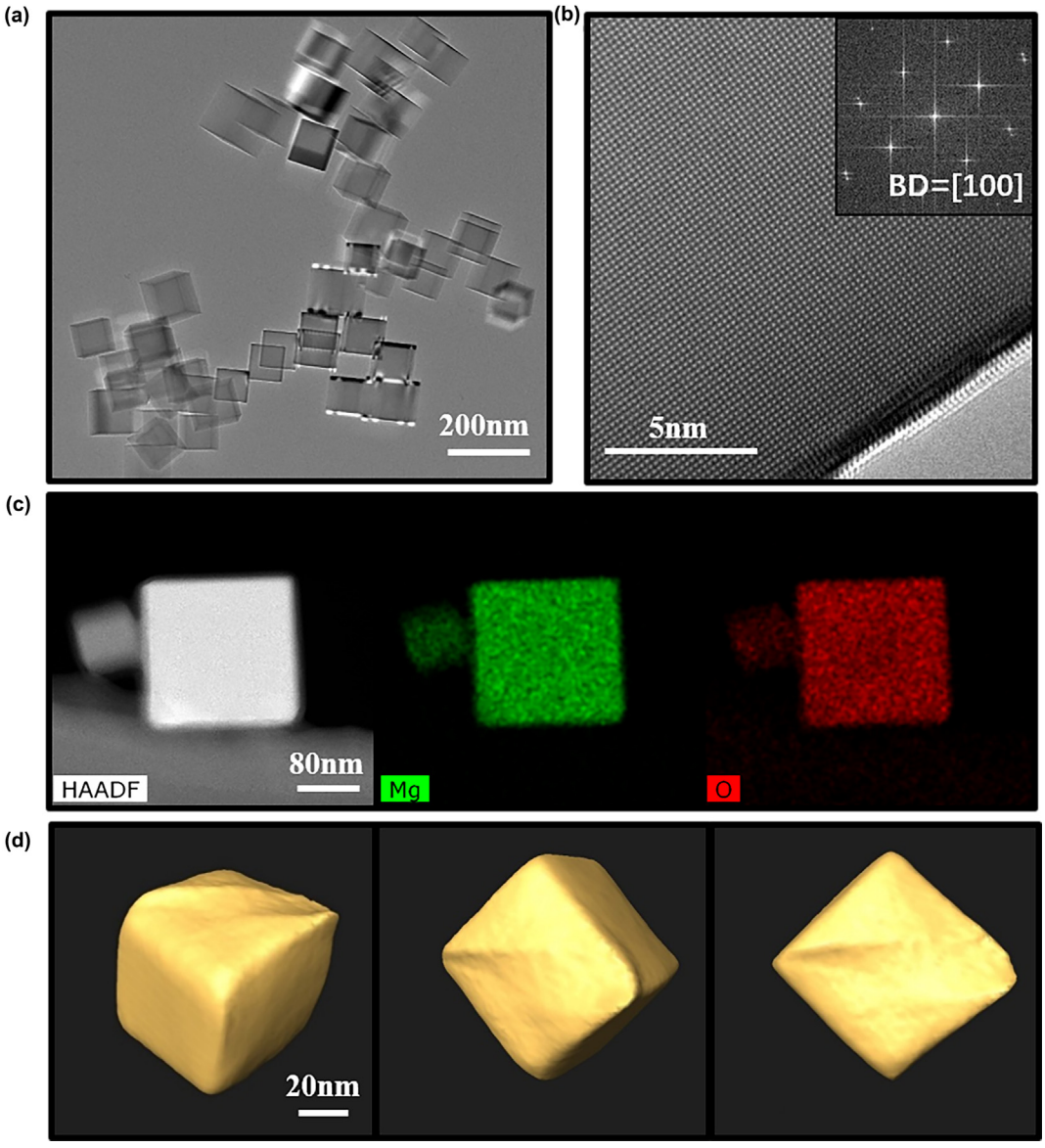

FIGURE 1

Characterization of the structure and morphology of MgO nanoparticles. (a) Bright-field TEM image of aggregated MgO nanoparticles. (b) HRTEM image of a typical MgO nanoparticle and the corresponding fast Fourier transform (FFT) pattern along the [100] beam direction. (c) STEM-HAADF image and EDS mappings of MgO nanoparticles. (d) 3D tomography of a MgO nanoparticle.

the electron irradiation condition in our experiment, they showed no significant change in the surface morphology after a certain time of electron irradiation (10 min for this sample). In stark contrast, NPs smaller than 100 nm were quite sensitive to electron irradiation. Under the same period of electron irradiation (10 min), brick-like nanostructures densely formed on the surface as shown in Fig. 2d. These nanostructures are of several nanometers and are distributed evenly. The significant effect of E-beam irradiation on smaller NPs could be due to a substantial increase in the peak current density by beam convergence and a relatively larger specific surface area [20].

The influence of electron irradiation on the mechanical properties of NPs has been investigated before. Mačković et al. [21] reported a significant increase in Young's modulus and strength of SiO_2 NPs after low-dose electron irradiation. Zang et al. [22] have shown that E-beam irradiation changes the elastic and electrical conductivity properties of crystalline zinc tin oxide nanowires. It had also been indicated that the densification of materials caused by E-beams is one of the factors that increase strength [21]. However, the underneath mechanism is still controversial. Since the degree to which the MgO NPs are affected by electron radiation varies with size, it is then of great interest to test if the change in surface morphology under the E-beam with size would result in different dislocation nucleation behaviors and therefore distinguished mechanical properties.

In situ TEM nano-compression tests on irradiated MgO NPs with different sizes and different degrees of surface modification were performed. As the study focused on the dislocation nucleation process, only particles containing no pre-existing dislocations were selected. The loading direction was along the same

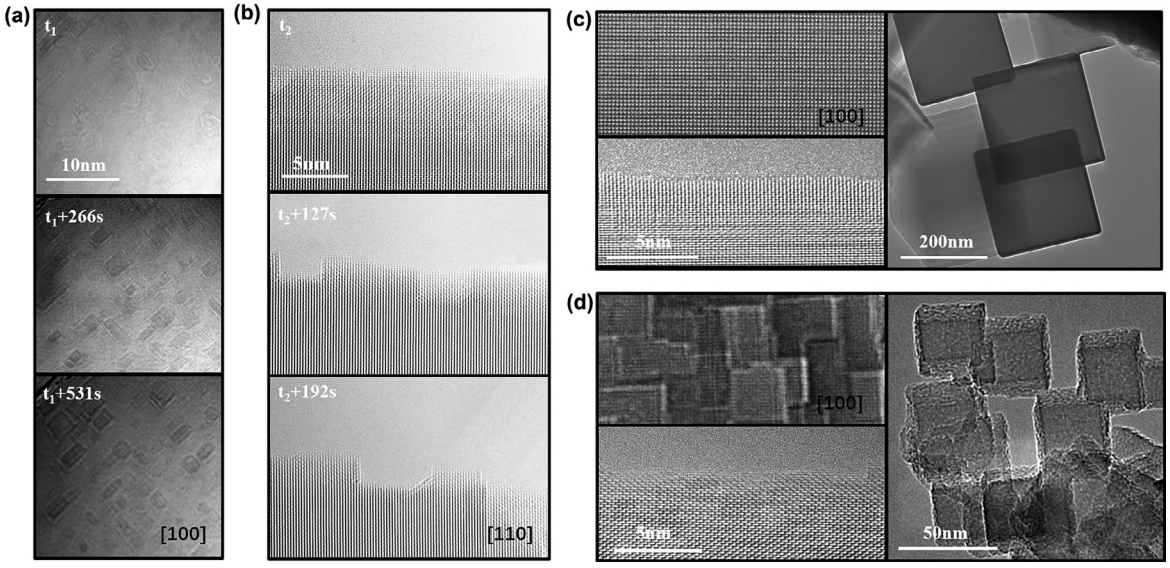

FIGURE 2

The effect of the E-beam on the MgO NPs. (a-b) Time sequence TEM images showing the surface nano-crystallization of MgO nanoparticles under electron irradiation. (c) HRTEM images (left) and bright-field TEM image (right) showing the morphology of MgO nanoparticles larger than 100 nm after the electron irradiation. d HRTEM image (left) and bright-field TEM image (right) showing the morphology of MgO nanoparticles smaller than 100 nm after the electron irradiation.

<100> orientation. Fig. 3a displays the corresponding engineering stress–strain curves for MgO NPs of sizes 320 nm, 260 nm, and 200 nm (side length) during the in-situ compression tests. The engineering stress was defined as the load applied by the nanoindenter over the initial contacting area. Fig. 3b are images captured from Movie 1, 2, and 3, showing the corresponding deformation process of the three MgO NPs. Compressive strength is the capacity of the material to withstand loads without fracture. The compressive strength of the three MgO is quite close and seems to be independent of particle size at this scale. They share resemble compressive strength, with values of 11.4 GPa, 11 GPa, and 8.9 GPa respectively, beyond which the particles underwent catastrophic shape change. Although the MgO NPs are dislocation-free before the compression tests, the value of their strength is far below the theoretical strength of MgO for this orientation (37 GPa) [15].

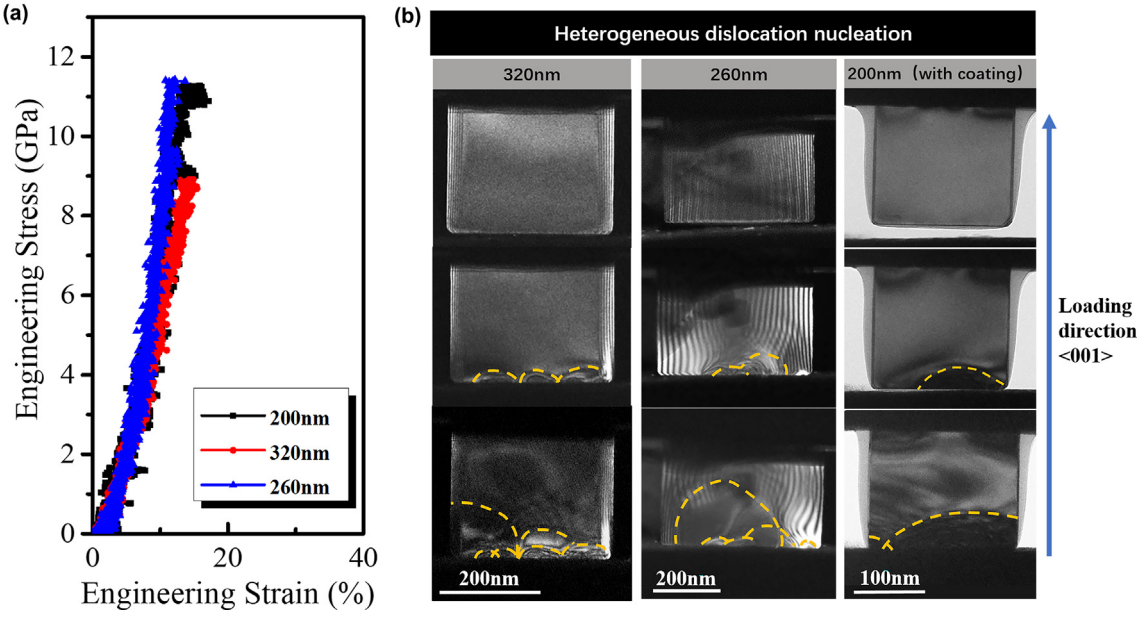

FIGURE 3

In-situ compression tests inside TEM on MgO nanoparticles larger than 100 nm. (a) Stress–strain curves for MgO nanoparticles of 320 nm, 260 nm and 200 nm in diameter. (b) TEM images captured from Movie 1, 2, and 3, showing the heterogeneous nucleation of dislocations from the surface of the three MgO nanoparticles during the compression tests.

It is found that the relatively low strength of these NPs results from the heterogeneous nucleation of dislocation. Fig. 3b sequentially shows the microstructure evolution of the three MgO NPs under compressive load. As local strain will influence the phase of the incident E-beam and cause local contrast differences during imaging, the stress distribution of the material can be reflected by stress fringes. Further, since stress concentration may provoke the nucleation of dislocations, the stress fringes can be utilized to predict the dislocation nucleation sites and their distribution. In Fig. 3b, the stress fringes are marked by yellow dashed lines. The first images in each column display the morphology of MgO NPs before compression. It can be deduced from the intact symmetry and uniform contrast that there were no pre-existing dislocations or pre-introduced stresses in the MgO NPs before the compression tests. As the indenter contacts the NPs, stress fringes began to emerge at certain places on the surface. The uneven distribution and asymmetry contour of the stress fringes indicate the presence of stress concentration in all the three MgO NPs during the in-situ compression tests, and the local stress concentration was not alleviated even when the indenter is completely pressed onto the sample. Based on previous three-dimensional reconstructions, the surface of the MgO NP is not smooth but has a certain degree of undulation. The raised areas on the surface contact the indenter first and result in significant stress concentrations. The stress concentration encourages heterogeneous dislocation nucleation at these places, leading to a strength that is far below the theoretical strength.

In stark contrast, for NPs smaller than 100 nm, whose surface morphology had been significantly modified by electron irradiation, the compressive strength is much higher, close to three times that of NPs larger than 100 nm, and even approaches the theoretical strength of MgO. Fig. 4b are images captured from Movie 4, showing the homogeneous nucleation of dislocations from the surface of a typical MgO NP under 100 nm. The strain contours start from the contact surface and evolve symmetrically as the indenter compresses into the MgO NP. They appear periodically on the surface with similar sizes and display symmetrical contours. The uniformly distributed strain fringes suggest relatively homogeneous dislocation nucleation. Until over 30 GPa of applied stress was reached, the catastrophic drop of the force occurred. More comparison tests on each size range were performed to ensure the reproducibility of the experiments (as shown in Fig. S5).

In both small NPs and large NPs, the particle collapsed rapidly with a remarkable increase in width at the yield point. The collapse of the particles corresponds to the multiple nucleation of dislocations on the surface and the following dislocation avalanche [23,24]. As shown in Fig. 4c, large numbers of dislocations were generated at the same time, dislocations that nucleate on different glide planes entangled with each other, resulting in high interior dislocation density in the deformed particles. The MgO NPs here are single crystals, so the dislocation avalanche extended to the entire cross-section of the sample [23].

Further, to draw a solid conclusion, we need to clarify that the increased strength with decreasing size of the dislocation-free MgO NPs is mainly caused by electron irradiation on the surface rather than the size effect. MgO NPs smaller than 100 nm were chosen and they were coated with carbon before the compression test to ensure that their surface won't be modified much by electron irradiation. It is noticeable that although the coated

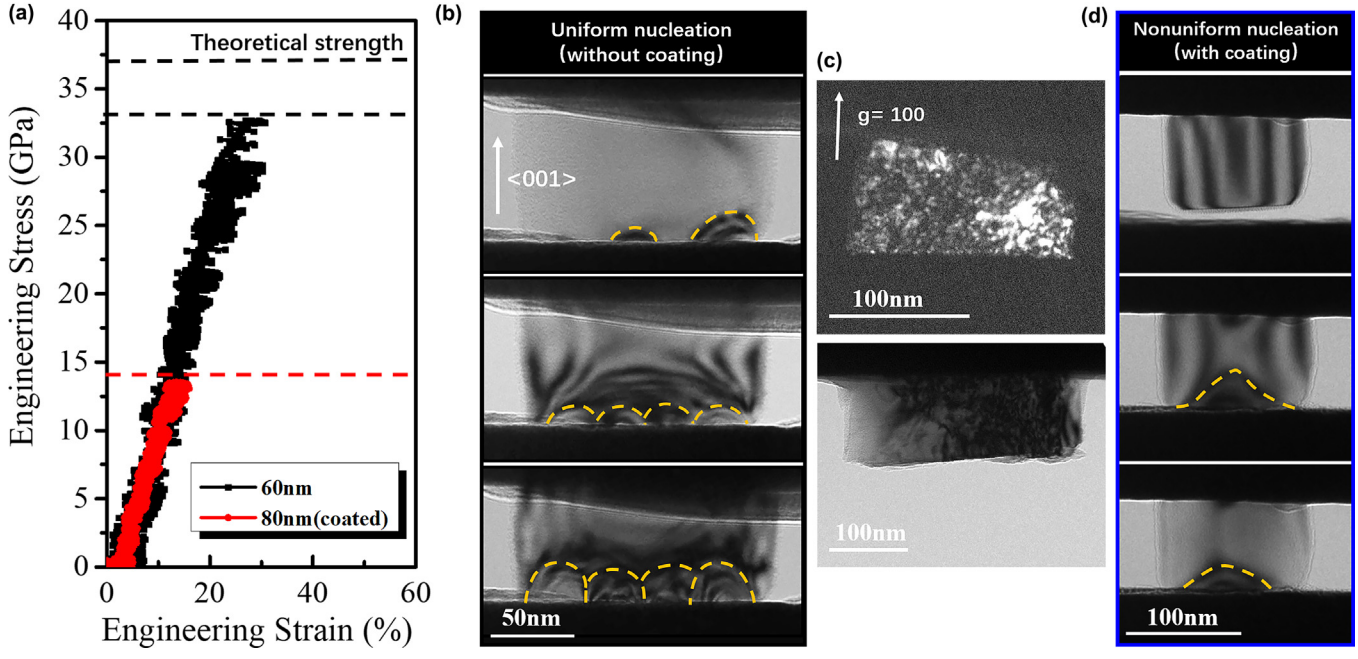

FIGURE 4

In-situ compression tests inside TEM on MgO nanoparticles smaller than 100 nm. (a) Stress–strain curves for MgO nanoparticles of 60 nm (without coating) and 80 nm (with coating) respectively. (b) TEM images captured from Movie 4, showing the homogeneous nucleation of dislocations from the surface of a MgO nanoparticle smaller than 100 nm. (c) Dark-field and bright-field TEM images of different sizes of NPs after the compression tests, showing the generation of large amounts of dislocations inside these NPs. (d) TEM images showing the heterogeneous nucleation of dislocations from the surface of an 80 nm MgO nanoparticle with carbon coating.

MgO NP is smaller than 100 nm, it shares similar strength (close to 13 GPa) with NPs larger than 100 nm, indicating that the strength of the MgO NP is almost irrelevant with size but highly depends on surface treatment. Further, there is almost no size effect when the influence of the E-beam is low. The 80 nm coated MgO NP is compared with a 200 nm coated MgO NP and the results are shown in Fig. S2. Although the two NPs are in different size levels, their compression strength is similar. Fig. 4a compares the engineering stress–strain curves of an 80 nm MgO nanoparticle with carbon coating (red curve) and a 60 nm MgO nanoparticle without coating (black curve). It is found that although the sizes of these two particles are similar, their mechanical properties are quite different. The coated nanoparticles collapsed at about 13 GPa, while the compressive strength of the nanoparticles without coating is as high as 32.5 GPa. The increased strength indicates that the surface nanometerization caused by E-beam irradiation has a great influence on the mechanical properties of the MgO NPs. As mentioned before, the E-beam modifies the surface of the MgO NP by displacement damage, which mainly leads to two effects, one is the preferential subduction of the protogenetic raised areas on the particle surface under electron irradiation, making the surface more uniform. Another effect involves the generation of nanostructures, which further unify the significant unevenness on the surface. However, under the protection of the carbon coating, the displacement of Mg and O is significantly suppressed. Therefore, the original uneven surface topography remained, causing a significant reduction in strength, as shown by the engineering stress–strain curves in Fig. 4a. Fig. 4d shows the structural evolution of the coated NP during the compression test. In stark contrast with particles without coating, where dislocations nucleated uniformly from the surface, the dislocation nucleation in the coated NP is non-uniform suggested by the unevenly distributed stress fringes. For the coated MgO NP, when the prominent bumps on the surface contacted the nanoindenter, inhomogeneous dislocation nucleation occurred, causing the strength to be much lower than the theoretical strength. While for those small MgO NPs without coating, the large surface imperfections were homogenized by the E-beam and uniform nanostructures formed on the surface. The uniformly distributed nanostructures bear the load together, which helps to avoid inhomogeneous dislocation nucleation.

As the E-beam is also utilized to observe the deformation process, its influence on the mechanical properties of the MgO NP during the compression tests is interested. Fig. S3 shows the engineering stress–strain curves and the corresponding deformation behaviors of NPs with E-beam on and off respectively. They both underwent the irradiation of the E-beam for 10 min before the compression tests. It is discovered that the two NPs share similar compressive strength, indicating that the E-beam during the compression tests has almost no effect on the deformation behavior of the MgO NP.

Although the stress is still lower than the theoretical strength of this material, the strength displayed above all regards the dislocation nucleation events but not the activation of pre-existing dislocations. To prove this important point, another test was performed by introducing several dislocations in the NP in advance and then compressing it, as shown in Fig. 5. One MgO NP with its top surface not perfectly aligned with the punch surface was chosen (~10° misalignment). During the first compression, one corner of the NP first touched the punch and deformed. Several dislocations were generated from that corner. Then, the second compression was performed to investigate the deformation behavior of MgO NP with these dislocations. As shown in Fig. 5a, the MgO NP shows much lower strength (the max stress is close to 8.8 GPa). It deforms continuously and uniformly with-

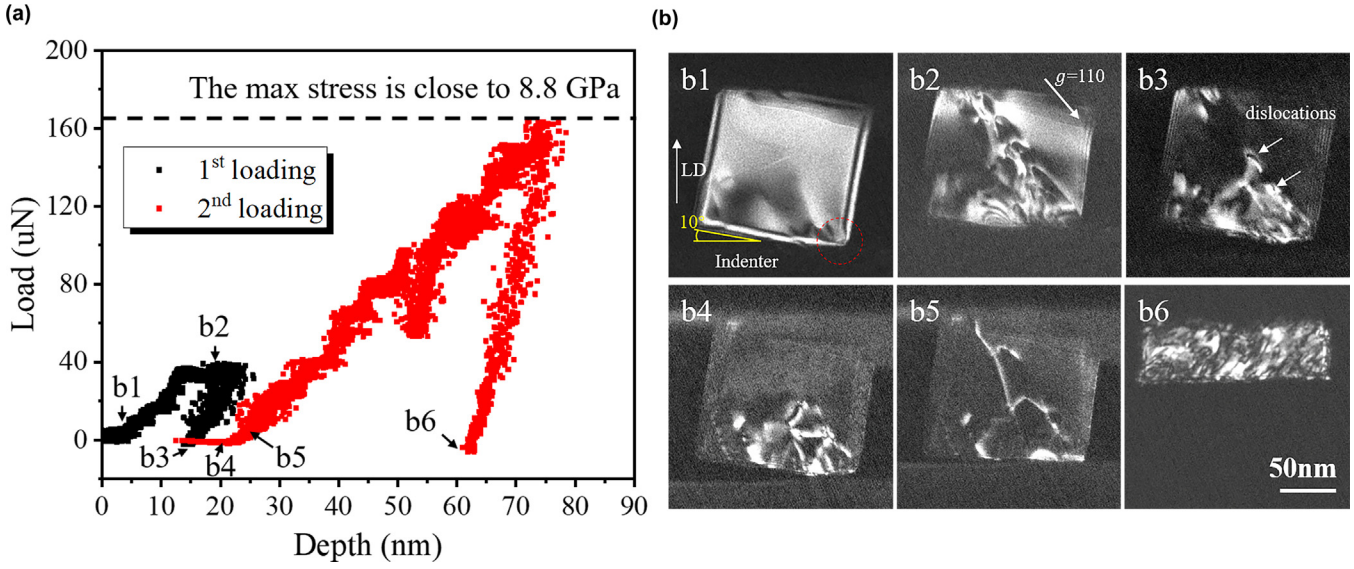

FIGURE 5

In-situ compression tests on a MgO NP showing lower strength and continuous deformability when dislocations are pre-introduced. (a) Load-depth curve. (b) Time-sequence TEM images (b1–b5) captured from Movie 5 and the deformed NP after unloading (b6), showing the deformation behavior of the MgO NP. The size of MgO NP is close to 136 nm. The dislocations were first introduced by compressing on one corner (position of red cycle) of the MgO NP. The NP was compressed again to investigate the deformation behavior of MgO NP with these pre-introduced dislocations.

out sudden burst or collapse. Fig. 5b is a series of images captured from Movie 5, dislocation slip was observed, providing for the continuous deformation with large plasticity of the MgO NP. The deformation mechanism of the MgO NPs with pre-existing dislocations is quite different from the particles tested before, where the NPs collapsed rapidly. The results suggest that the compressive strength for the previously tested NPs is related to the dislocation nucleation events instead of the activation of pre-existing dislocations.

To further reveal the effect of different surface conditions on intrinsic nucleation behaviors of MgO NPs, numerical simulations were performed to investigate the stress distributions of a set of MgO model samples with different surface conditions under uniaxial compression by finite element method through the commercial finite element analysis software, ABAQUS/Standard. Fig. S4 and Table 1 in the supporting information (SI) provide details of the samples and simulations. Two groups of samples with different surface bump sizes (r) and density (L/r) were selected to illustrate the influence of surface roughness on the stress distribution and thereby the dislocation nucleation behaviors, where r is the radius of the bump and L is the center distance between two neighbored bumps. Samples in the first group have the surface bump radius of 10 nm and density (L/r) of 2, 4 10 respectively. Samples in the second group have the sur-

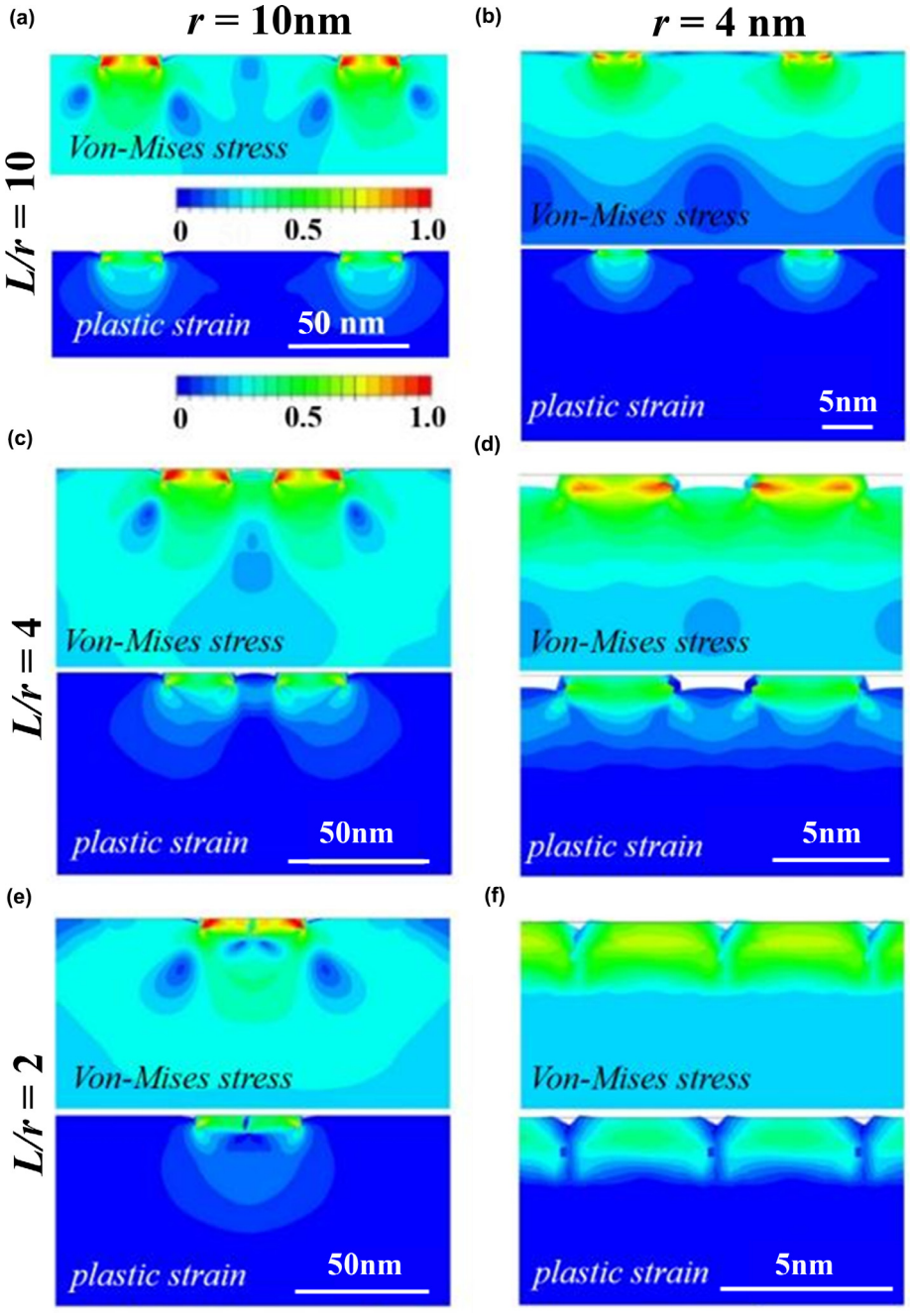

FIGURE 6

The distribution of calculated reduced Von-Mises stress and plastic strain of MgO model samples with various surface bump sizes (r) and density (L/r).

face bump radius of 4 nm and density (L/r) of 2, 4, and 10 respectively. The distributions of calculated reduced Von-Mises stress and plastic strain are shown in Fig. 6. In both cases, the distribution of stress becomes more heterogeneous as the bump density decreases. It is also discovered that under the same bump size, stress localization (hotspots) becomes more obvious as the density of the bumps (L/r) decreases until the stress fields of the bumps are totally separated. For samples with low density (L/r = 10), like in Fig. 6a and b, the bumps are secured from each other when being loaded, resulting in isolated stress fields. While for those with higher density (L/r = 4 or 2) as shown in Fig. 6c, d, e, and f, the stress fields generated by the bumps interact with each other, resulting in a more uniform stress distribution. Besides, the stress and plastic strain distribution of samples with high-density small bumps on the surface are relatively homogeneous, in consistent with experimental results, where surface nano-crystallization of the ceramic MgO sample results in relatively homogeneous surface stress distribution. Fig. 6a and Fig. 6f represent the two cases in the experiment. The bumps of samples in Fig. 6a are big and sparse, which is similar to the situation of the primary MgO NPs in the experiment. In this case, highly localized hotspots occur at the edges of large bumps, which is in favor of inhomogeneous dislocation nucleation. While for samples with small and dense bumps on the surface (Fig. 6f), which corresponds to the electron irradiation treated samples with the homogenized surface, the stress distribution and plastic strain are relatively uniform, providing a more uniform activation probability of dislocations. The above numerical simulation results provide a reasonable interpretation that homogeneous dislocation nucleation is the intrinsic behavior of MgO NPs with uniform nano-sized surface structures.

Discussion

The theoretical strength of a material is the stress required to deform an initially defect-free crystal. It involves the homogeneous, barrier-free nucleation of dislocations in a perfect crystal without any defects [25]. In real NPs, the nature of the uneven surface causes stress concentration and provides predominant nucleation sites, which increases the probability of heterogeneous dislocation nucleation and structural instability of the NPs. Since the stress concentration already raised the local stress to be high enough at the predominant sites for the heterogeneous dislocation nucleation to occur, the samples yielded at relatively low stress. Common attempts have been made to push the strength limits of materials by minimizing defects [26–28]. Here we propose an alternate approach to improve strength by simply homogenizing and miniaturizing the defects. Electron irradiation is utilized to endow the original rough surface of MgO NPs with nano-scale patterns, leading to a more uniform stress distribution and homogeneous nucleation of dislocations. In the case where surface imperfection can be reduced to nanoscale and distributed uniformly, large numbers of nucleation sites can operate simultaneously, therefore the applied stress that the material can afford would be much higher and even approach the same level of theoretical strength. The simulation results achieved by the finite element method illustrate that samples with small, dense bumps on the surface display relatively homogeneous stress distributions compared to those with large, sparse bumps on the surface, which is consistent with the experimental results.

It is also supported by other simulation results that surface morphology truly has a great influence on the stress distribution of the samples. Amodeo et al. [29] show that the impact of shape on the strength of $L1_2Ni_3Al$ NP is significant. Smoothing of corners and edges of originally cubic particles was proved to cause a strengthening effect by avoiding stress concentration. Further, Sharma et al. [28] suggest through molecular dynamics simulations that, uniform stress distribution encourages homogeneous dislocation nucleation inside the particle, which requires a higher level of the applied stress to reach the critical resolve shear stress. Here in our experiment, the nanostructures formed under electron irradiation homogenize the surface roughness, which alleviates stress concentration and creates a higher probability of homogeneous dislocation nucleation, making the MgO NP stronger. In addition, the stress field generated by these nanostructures can also influence and interact with each other. Models and simulations [30] indicate that such asperity interactions play an important role in governing mechanical behaviors. Surface texturing can influence stress distribution and thus suppress the nucleation and propagation of dislocations. The dislocations nucleated at the rough surface will stay in equilibrium position close to surface steps and remain trapped near the surface, which would generate a thin tensile-stress sub-layer adjacent to the surface that acts to increase the mean contact pressure.

In our experiments, since only the E-beam in TEM was used to perform the surface modification on every single particle every time, the dose was not high enough to affect the large particles. Only the small particles below 100 nm can be tuned. However, it indicates that if we tune the surface roughness precisely and homogenize the surface defects, quasi-homogeneous nucleation of dislocation on the surface can be achieved and utilized to optimize the strength of nanomaterials. A stronger E-beam can be used to modify larger samples and even the surface nanopatterns can be written more precisely by design. Homogenizing the defects is a distinctive strategy compared to the traditional paradigm of improving materials through defects minimization. It opens a new way to the design of stronger materials.

Methods

In-situ compression tests inside TEM

The in-situ compression tests were carried out with a Hysitron Picoindenter (PI95) inside a JEOL 2100F TEM in displacement-control mode and the displacement rate was 2 nm/s. Calibration was performed before nano-compression and the threshold load values for machine noise was ~−1 μN to 1 μN. The MgO NPs were placed on a silicon wedge (width for ~2 μm) which was glued to a substrate. Individual MgO NP was compressed by a diamond flat tip (5 μm in diameter), while the dislocation nucleation process was simultaneously observed by looking at the evolution of strain contours in a TEM; quantitative load–displacement (L–D) data were recorded during compression tests; in-situ movie and high-resolution TEM images of the regions of interest were recorded with a Gatan 833 CCD camera at 10 frames per second.

3D electron tomography

The tomography was performed in a Titan G2 microscope using a single tilt holder (Fischione 2020), operated at 300 kV. HAADF-STEM images were acquired at a tilting range of ±64° every 2°. Reconstruction was performed by FEI Inspect 3D software. Segmentation and visualization of the reconstructed 3D volume were carried out using FEI Amira software.

Numerical simulations

Two-dimensional plane strain boundary layer formulation is employed in all simulations. The model MgO NPs are represented by the 250 × 150 nm^2 rectangular samples with hemispheric bumps on the surface. The roller boundary condition is applied to the bottom and on both sides of the sample. An analytical rigid indenter with a length of 250 nm is used to apply compression on the upper surface of the samples. Four-node bilinear plane strain quadrilateral elements with reduced integration (CPE4R) are used for mesh generation. The size of each element is approximately 0.2 nm, which discretizes the whole model into about 940,000 elements. The elastic linear-hardening material model is chosen in representing MgO, which stress–strain relation can be written as:

$$\sigma_e = \begin{cases} E\varepsilon_e \ (\sigma_e \leqslant \sigma_y) \\ \sigma_y + E_p(\varepsilon - \varepsilon_y) \ (\sigma_e > \sigma_y) \end{cases}$$

where E_p is the tangent modulus, and $\varepsilon_y = \frac{\sigma_y}{E}$ is the yield strain. Other modeling parameters are listed in Table S1.

CRediT authorship contribution statement

Sijing Chen: Conceptualization, Investigation, Validation, Formal analysis, Writing – original draft, Writing – review & editing. **Fei Liu:** Investigation, Validation, Formal analysis, Writing – review & editing. **Boyu Liu:** Conceptualization, Supervision, Formal analysis, Writing – review & editing, Funding acquisition. **Xiao Chen:** Resources, Investigation. **Xiaoxing Ke:** Investigation, Formal analysis, Funding acquisition. **Manchen Zhang:** Investigation, Formal analysis, Funding acquisition. **Xiaochang Tang:** Investigation, Formal analysis. **Pengfei Guan:** Investigation, Validation, Formal analysis. **Ze Zhang:** Supervision, Writing – review & editing. **Zhiwei Shan:** Supervision, Writing – review & editing, Funding acquisition. **Qian Yu:** Conceptualization, Methodology, Supervision, Project administration, Investigation, Validation, Writing – review & editing, Funding acquisition.

Declaration of Competing Interest

The authors declare that they have no known competing financial interests or personal relationships that could have appeared to influence the work reported in this paper.

Acknowledgements

Q.Y. acknowledges support by National Natural Science Foundation of China (51671168, and 51871197), the National 111 project under grant No. B16042, and the State Key Program for Basic Research in China under grant no 2017YFA0208200. Z.W.S. and B.Y.L. acknowledge the support provided by National Natural Science Foundation of China (52031011, 51971168, 52022076) and 111 Project 2.0 (BP0618008). X.K. M.Z. acknowledge support by National Natural Science Foundation of China (12074017, 51621003). P.F.G. acknowledges financial support by the National Natural Science Foundation of China (Grant No. U1930402) and the computational support from the Beijing Computational Science Research Center (CSRC). We thank Dr. Y.B. Qin, Dr. C.W. Guo, and Dr. P. Zhang from Xi'an Jiaotong University for assistance in sample preparation and TEM experiments.

Author contributions

Q.Y. and B.Y.L. designed the experiments and directed the project. X.C. synthesized the MgO nanoparticle, S.J.C. and F.L. performed the in situ TEM experiments (supervised by Q.Y. and B.Y.L.). X.X.K. and M.C.Z conducted the 3D tomography, X.C.T. and P.F.G. performed the numerical simulations. S.J.C., F.L., Q.Y. and B.Y.L. performed the data analysis and wrote the manuscript. Q.Y., B.Y.L., Z.Z and Z.W.S provided supervision of all studies; all authors contributed to the discussion and revision of the paper.

Data availability

The data that support the findings of this study are available from the corresponding author upon reasonable request.

Appendix A. Supplementary data

Supplementary data to this article can be found online at https://doi.org/10.1016/j.mattod.2022.04.007.

References

[1] Q. Wu et al., Nanotechnol. Rev. 9 (2020) 259–273.
[2] M.M. Modena et al., Adv. Mater. 31 (2019) 1901556.
[3] D. Guo, G. Xie, J. Luo, J. Phys. Appl. Phys. 47 (2014) 013001.
[4] T.A. Saleh, Environ. Technol. Innov. 20 (2020) 101067.
[5] K. Niwase, Quantum Beam Sci. 5 (2021) 4.
[6] L. Nicola et al., J. Mech. Phys. Solids 55 (2007) 1120–1144.
[7] L.Y. Chen et al., Nat. Mater. 14 (2015) 707–713.
[8] D. Mordehai, O. David, R. Kositski, Adv. Mater. 17 (2018).
[9] S.P. Venugopalan, L. Nicola, Acta Mater. 165 (2019) 709–721.
[10] G.E. Norman, A.V. Yanilkin, Phys. Solid State 53 (2011) 1614–1619.
[11] T. Zhu et al., Phys. Rev. Lett. 100 (2008) 025502.
[12] Q.-J. Li et al., Acta Mater. 145 (2018) 19–29.
[13] Z.-J. Wang et al., Acta Mater. 60 (2012) 1368–1377.
[14] W.-Z. Han et al., Adv. Mater. 27 (2015) 3385–3390.
[15] C.B. Carter, M.G. Norton, Ceram. Mater. (Springer New York 2013). Doi: 10.1007/978-1-4614-3523-5.
[16] S. Wang et al., Metall. Mater. Trans. A 51 (2020) 2957–2974.
[17] I. Issa et al., Acta Mater. 86 (2015) 295–304.
[18] H.-R. Zhang, R. Egerton, M. Malac, Nucl. Instrum. Methods Phys. Res. Sect. B Beam Interact. Mater. At. 316 (2013) 137–143.
[19] T. Kizuka, Jpn. J. Appl. Phys. 40 (2001) L1061–L1064.
[20] P.S. Turner et al., Philos. Mag. Lett. 61 (1990) 181–193.
[21] M. Mačković et al., Acta Mater. 79 (2014) 363–373.
[22] J. Zang et al., Nano Lett. 11 (2011) 4885–4889.
[23] F.F. Csikor et al., Science 318 (2007) 251–254.
[24] T. Crosby et al., Acta Mater. 89 (2015) 123–132.
[25] H. Wang, Theoretical strength of solids. (2010).
[26] Z. Zhou, H. Wang, M. Li, Phys. Rev. B 100 (2019) 024109.
[27] A. Nie et al., Nat. Commun. 10 (2019) 5533.
[28] A. Sharma et al., Nat. Commun. 9 (2018) 4102.
[29] J. Amodeo, K. Lizoul, Mater. Des. 135 (2017) 223–231.
[30] J. Guo et al., Appl. Surf. Sci. 539 (2021) 148277.